Measurement 172 (2021) 108976

Contents lists available at ScienceDirect

Measurement

journal homepage: www.elsevier.com/locate/measurement

Feature extraction method based on adaptive and concise empirical wavelet transform and its applications in bearing fault diagnosis

Kun Zhang [a,b], Chaoyong Ma [b,*], Yonggang Xu [b], Peng Chen [a], Jianxi Du [b,c]

[a] Graduate School of Environmental Science and Technology, Mie University, Tsu 514-0001, Japan
[b] The Key Laboratory of Advanced Manufacturing Technology, Beijing University of Technology, Beijing 100124, China
[c] Beijing Huahang Radio Measurement Institute, Beijing 100000, China

ARTICLE INFO

Keywords:
Empirical wavelet transform
Feature extraction
Weighted unbiased autocorrelation
Signal processing
Fault diagnosis

ABSTRACT

Empirical wavelet transform is good at distinguishing components containing different frequency information in complex signals. Due to the higher complexity of the Fourier spectrum, the original method would generate a large number of boundaries, more invalid components. The division method without considering the fluctuation characteristics will affect the results. In this paper, adaptive and concise empirical wavelet transform (ACEWT) is proposed. The power spectral density of the signal is calculated and used to segment the spectrum, which can reduce the number of extreme points and the dependence on them in the original method. Weighted unbiased autocorrelation (WAC) that can filter bearing fault information is proposed. After combining ACEWT and WAC, a tower boundaries distribution diagram (W-Autogram) which can be used to extract specific information is proposed. Simulation signals and experimental results verify that the proposed method can be applied to the fault diagnosis of rolling bearings in rotating machinery.

1. Introduction

Signal processing methods are widely used in many fields, such as medical equipment, military equipment, industrial engineering equipment, road monitoring, and so on. Therefore, the proposal and development of signal processing methods are closely related to the daily life of human beings. Rotating machinery is widely used in daily life, such as various types of engines, turbines, centrifuges, lathes, fans, propellers, etc. With the development of industrial automation and intelligence, more and more rotary equipment has been applied. The requirements for the quality of rotating parts in equipment become higher and more stringent. High pressure resistance, high temperature resistance, and high load resistance are the most basic requirements for enterprises. Non-intermittent work and a longer normal working cycle become the core requirements. If early failures of rotating components such as bearings and gears are not detected, it is easy to cause the equipment to stop and be dangerous [1,2]. For this reason, it is necessary to perform health monitoring or troubleshooting of rotating equipment.

When dealing with complex simulation signals or acquired signals that may contain faults, modal aliasing and endpoint effects are issues that traditional methods must face to be solved. The traditional signal processing methods could be divided into time–frequency analysis method and mode decomposition method. Time-frequency analysis methods usually require preset time–frequency resolution. The proper combination of time resolution and frequency resolution can show the signal characteristics in a two-dimensional graph [3]. For example, the short-time Fourier transform can show the change in frequency after the window function is set in advance. However, it takes experience when presetting parameters and the tedious steps will bring more workload and not necessarily achieve the desired results. The traditional mode decomposition methods represented by wavelet transform and empirical mode decomposition have developed rapidly. The decomposition process of wavelet transform is easy to be explained by theory, but it is difficult to achieve self-adaptation [4]. Similar to the time–frequency analysis method, the wavelet transform needs to select a suitable wavelet basis function. However, this method inevitably causes energy leakage, which is the most fundamental reason for the modal aliasing of the method. In order to increase the adaptability of signal processing, Huang [5] proposed empirical mode decomposition (EMD). EMD relies on extreme points of signal fluctuations. During each modal separation, the median of the maximum and minimum series is considered as separate components. However, noise and non-stationary signals are

* Corresponding author.
E-mail addresses: zkun212@163.com (K. Zhang), machaoyong_bjut@163.com (C. Ma), xyg_1975@163.com (Y. Xu), chen@bio.mie-u.ac.jp (P. Chen), djx12016@163.com (J. Du).

https://doi.org/10.1016/j.measurement.2021.108976
Received 24 August 2020; Received in revised form 24 December 2020; Accepted 29 December 2020
Available online 6 January 2021

difficult to meet the prerequisites for EMD implementation [6], which has led to a series of data-driven mode decomposition methods such as local mean decomposition that are prone to endpoint effects and modal aliasing [7,8]. Modal aliasing is manifested in the time domain as having periodic waveforms between different components, and in the frequency domain, the manifestation is that different components contain the same frequency component. Variable speed conditions may have crossovers with other components in the frequency spectrum, so they are outside the scope of this article.

Chen [9,10] proposed a new idea of segmenting signals from the spectrum——analytical mode decomposition(AMD). AMD can split the signal into high and low frequencies based on the selected frequency. However, how to preselect the frequency is a problem that needs to be solved. In addition, Gilles [11] proposed a similar idea based on Meyer wavelet and named it empirical wavelet transform(EWT). EWT also divides the signal in the spectrum. The maximum and minimum of the spectrum are used by Gilles to distinguish useful modes. In earlier versions, the midpoint or minimum of adjacent maxima was used as the boundaries [12]. EWT was quickly applied after it was proposed. Premjith [13] uses EWT for Audio Data Authentication. Jiang [14] used EWT to separate the part of the bearing signal containing inner ring fault and outer ring fault, and then used the duffing oscillator to identify the fault information. EWT is also used to judge internal fault current and inrush current in a power transformer [15]. Chen [16] combined clustering and EWT to suppress strong noise in seismic signals. In addition, EWT is also applied to hyperspectral image classification [17], inspecting debonding defects [18], and so on. It is widely used in rotating equipment such as wind turbine [19], motor bearing [20], bearing with varying speeds [21], and railway axle bearing [22]. Kedadouche [23] proved through simulation and experimental signals that EWT is more effective than EMD in processing bearing fault. The above methods have good results when processing clean or stationary signals, but it is difficult to successfully segment complex signals [24]. In order to reduce parameter input and increase the adaptability of EWT, Gilles [25] proposed a parameterless method based on scale-space in 2014 to find useful modes from histograms. Otsu's method and k-means method are used as reference for readers. After this method was proposed, it was quickly and successfully applied to bearing fault diagnosis [26] and rotor rubbing fault diagnosis [27]. Pan [28] found a suitable scale space curve with pre-determined scale parameter through a large number of experiments. Pearson's correlation coefficient is cited to filter components with fault information [26,28]. Amezquita - Sanchez [29] uses multiple signal classification to calculate the new spectrum, and treats the minimum value near the maximum value as the boundaries after zeroing the part below the threshold.

If only extreme points are considered, but the relationship between the spectral fluctuation characteristics and the signal is ignored, new problems will appear. With the improvement and upgrade of data acquisition equipment, high sampling frequency and big data analysis have also developed. Due to the higher complexity of the Fourier spectrum, the number of extreme points is greatly affected by the sampling frequency. When analyzing signals with long data, the original method will reduce the quality of the components and affect the effectiveness and efficiency of diagnosis. In order to reduce the number of invalid components and suppress modal aliasing, this paper proposes an adaptive and concise empirical wavelet transform (ACEWT). First, the power spectral density (PSD) of the signal is calculated and used to separate the modes. On the one hand, it can reduce the number of extreme points and weaken the dependence on extreme points; on the other hand, the fluctuation of PSD corresponds to the concentration of different components in the signal, which provides a basis for the process of segmenting the spectrum. In order to expand the application of this method, this paper implements adaptive spectral segmentation by constructing a new tower boundaries distribution diagram. The optimized diagram contains different levels of segmentation, and the spectrum would be divided into several frequency bands with different widths. Scholars can extract information of interest from this diagram according to specific methods. This paper mainly extracts the periodic pulse information in the signal, and the fault information in the rotating machinery, especially the rolling bearing signal, to provide a new method for fault diagnosis.

Moshrefzadeh [30] used the unbiased autocorrelation (AC) of the squared envelope of the demodulated signal to take advantage of the cyclic stationary characteristics of the bearing fault signal. The tower boundaries distribution diagram (W-Autogram) proposed in this paper may have narrow frequency bands when the sampling frequency is large. The reconstructed waveforms of such frequency bands are likely to contain pulses and affect the sensitivity of AC. In addition, the fault information of the bearing signal is often concentrated around a center frequency in the Fourier spectrum. The more sidebands and less noise the component contains, the easier it is to find faults. Narrow frequency bands containing pulses are usually interference information. In order to filter the fault information in W-Autogram, this paper proposes a weighted unbiased autocorrelation (WAC) that correlates the index and the bandwidth. Simulation signals and experimental results verified that the proposed method can not only extract periodic pulses from noise, but also diagnose faults in the inner and outer rings of rolling bearings in rotating machinery. The structure of the paper is as follows: Section 2 introduces the EWT method; Section 3 uses simulation signals to explain the details of the proposed adaptive and concise empirical wavelet transform, weighted unbiased autocorrelation, and W-Autogram; Section 4 applies this method to rolling bearing fault diagnosis.

2. Empirical wavelet transform

The essence of empirical wavelet transform is a set of filters based on Meyer wavelet, which can decompose the signal into several components. The Fourier spectrum is calculated and normalized to $[0,\pi]$. A parameterless method based on scale-space representation can calculate a set of boundaries that may divide the spectrum into plenty of parts. Each frequency band is defined as a useful mode. Provided that the number of useful modes is defined as N, set ω as boundaries calculated by scale-space method among the bands: $\omega_0 = 0$, $\omega_N = \pi$. The first and second frequency bands can be expressed as $\Lambda_1 = [\omega_0, \omega_1]$, $\Lambda_2 = [\omega_1, \omega_2]$. Set $n = 1, 2, \cdots, N$, $\Lambda_n = [\omega_{n-1}, \omega_n]$, The spectrum can be expressed as: $\bigcup_{n=1}^{N}\Lambda_n = [0,\pi]$.

EWT will construct a band-pass filter for each frequency band. There is a transition phase between adjacent filters. The transition phase is centered at ω. $2\tau_n$ is the width. The basic structure of the filter is: the transition phase is a set of mutually orthogonal trigonometric functions, and the center of the frequency band is constant. The empirical scaling function $\widehat{\varnothing}_n(\omega)$ and the empirical wavelets $\widehat{\Psi}_n(\omega)$ can be defined as [11]:

$$\widehat{\varnothing}_n(\omega) = \begin{cases} 1; |\omega| \le (1-\gamma)\omega_n \\ \cos\left[\frac{\pi}{2}\beta\left(\frac{1}{2\gamma\omega_n}(|\omega| - (1-\gamma)\omega_n)\right)\right]; \\ (1-\gamma)\omega_n \le |\omega| \le (1+\gamma)\omega_n \\ 0; others \end{cases} \tag{1}$$

$$\widehat{\Psi}_n(\omega) = \begin{cases} 1; (1+\gamma)\omega_n \le |\omega| \le (1-\gamma)\omega_{n+1} \\ \cos\left[\frac{\pi}{2}\beta((|\omega| - (1-\gamma)\omega_{n+1})/2\gamma\omega_{n+1})\right]; \\ (1-\gamma)\omega_{n+1} \le |\omega| \le (1+\gamma)\omega_{n+1} \\ \sin\left[\frac{\pi}{2}\beta((|\omega| - (1-\gamma)\omega_{n+1})/2\gamma\omega_n)\right]; \\ (1-\gamma)\omega_n \le |\omega| \le (1+\gamma)\omega_n \\ 0; others \end{cases} \tag{2}$$

where the transition function $\beta(x)$, the coefficient γ, and the transition

phase τ_n are:

$$\beta(x) = x^4(35 - 84x + 70x^2 - 20x^3) \tag{3}$$

$$\gamma < min\left(\frac{\omega_{n+1} - \omega_n}{\omega_{n+1} + \omega_n}\right) \tag{4}$$

$$\tau_n = \gamma\omega_n, 0 < \gamma < 1 \tag{5}$$

Set the Fourier transform as $F(\cdot)$, the inverse Fourier transform is $F^{-1}(\cdot)$. The detail coefficients W_f^ε can be defined as:

$$W_f^\varepsilon(n,t) = < f(t), \Psi_n(t) >$$

$$= \int f(\tau)\overline{\Psi_n(\tau - t)}d\tau = F^{-1}\left(\hat{f}(\omega)\hat{\Psi}_n(\omega)\right) \tag{6}$$

Calculate the approximation coefficients $W_f^\varepsilon(0,t)$:

$$W_f^\varepsilon(0,t) = < f(t), \varnothing_1(t) >$$

$$= \int f(\tau)\overline{\varnothing_1(\tau - t)}d\tau = F^{-1}\left(\hat{f}(\omega)\hat{\varnothing}_1(\omega)\right) \tag{7}$$

where $\hat{f}(\omega)$, $\hat{\varnothing}_1(\omega)$, $\hat{\Psi}_n(\omega)$ are the Fourier transforms of $f(t)$, $\varnothing_1(t)$, and $\Psi_n(t)$.

The signal can be rebuilt as follows:

$$f(t) = W_f^\varepsilon(0,t) * \varnothing_1(t) + \sum_{n=1}^{N} W_f^\varepsilon(n,t) * \Psi_n(t)$$

$$= \mathrm{F}^{-1}\left(\widehat{\mathrm{W}}_{\mathrm{f}}^{\varepsilon}(0,\omega)\hat{\varnothing}_1(\omega) + \sum_{\mathrm{n}=1}^{\mathrm{N}} \widehat{\mathrm{W}}_{\mathrm{f}}^{\varepsilon}(\mathrm{n},\omega)\hat{\Psi}_{\mathrm{n}}(\omega)\right) \tag{8}$$

where $\widehat{W}_f^\varepsilon(0,\omega)$ and $\widehat{W}_f^\varepsilon(n,\omega)$ are the Fourier transforms of $W_f^\varepsilon(0,t)$ and $W_f^\varepsilon(n,t)$. The empirical mode could be given by:

$$\begin{cases} f_0(t) = W_f^\varepsilon(0,t) * \varnothing_1(t) \\ f_k(t) = W_f^\varepsilon(k,t) * \Psi_k(t) \end{cases} \tag{9}$$

3. Adaptive and concise empirical wavelet transform

Section 2 introduces the basic principles of EWT. In the process of calculating the modes, the most critical step is to obtain the boundaries. The number and location of the boundaries determine the number and quality of the modes. Fig. 1a shows the flowchart of EWT. Since the Fourier spectrum contains a large number of extreme points, the number of local maxima may be greater. In order to improve EWT, Section 3.1 proposes a mode decomposition method based on power spectral density. Its flowchart is shown in Fig. 1b. In order to expand the application of ACEWT, we propose a new indicator in Section 3.2. After weighting the unbiased autocorrelation, this indicator becomes more sensitive to periodic pulse information. Further, by combining ACEWT and Weighted AC, a tower boundaries distribution diagram (W-Autogram) which can be used to extract specific information is proposed. Fig. 1c shows the flowchart of W-Autogram and the location of the details of each part in the paper.

3.1. The mode decomposition method based on power spectral density

The original EWT method segments the Fourier spectrum through the scale-space representation. For noise-free signals, EWT can separate different components well. But in reality, it is difficult to avoid noise. Since the signals usually belong to a non-stationary state, it brings difficulties to EWT. The Fourier spectrum displayed is usually related to the size of the sampling frequency. The higher the sampling frequency, the more detailed the information in the signal. Similarly, the signal would

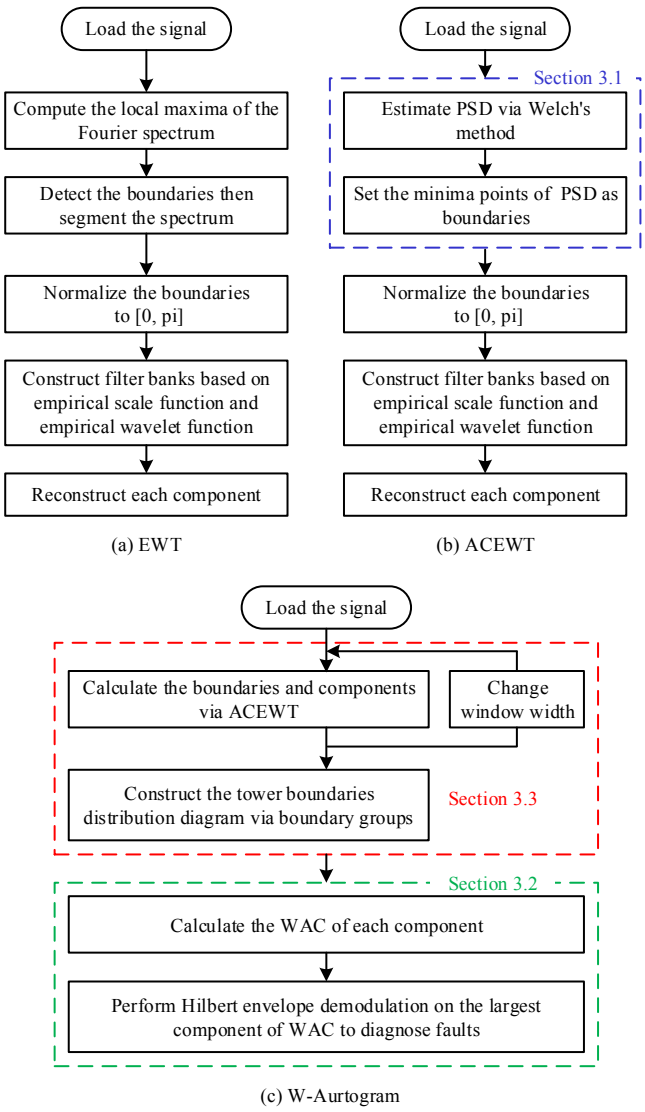

Fig. 1. The flowcharts of the proposed methods.

be more complex, which brings more work to the scale-space representation. This section uses PSD to replace the complex Fourier spectrum to show the distribution of components.

PSD actually represents the distribution of power with frequency. For the signal $y(t)$, the Fourier transform is $\hat{y}(f)$, and its average power P can be expressed as:

$$P = \lim_{T\to\infty} \frac{1}{2T}\int_{-T}^{T} y(t)^2 dt \tag{10}$$

Provided that the Fourier transform of the signal in the interval $[0, T]$ is:

$$\hat{y}_T(f) = \frac{1}{\sqrt{T}}\int_0^T y(t)e^{-i2\pi ft}dt \tag{11}$$

Then the power spectral density can be defined as [31]:

$$S_{yy}(f) = \lim_{T\to\infty} E\left[|\hat{y}_T(f)|^2\right] \tag{12}$$

It can be found from Eq.12 that PSD is a positive number greater than zero and is a frequency-dependent spectrum. There are several sets of simulation signals showing the relationship between the PSD and the fluctuation trend of the spectrum.

The first component is a modulation signal:$f_1 = 10$ Hz, $f_2 = 100$ Hz.

The second component is a cosine: $f_3 = 400$ Hz. The third component is the periodic pulses. The natural frequency of the pulse is $f_n = 1600$ Hz, the sampling frequency $f_s = 10000$ Hz, the damping coefficient $g = 0.02$ and the repetition period $T = 0.03$ s. The simulated signal and its components are shown in Fig. 2. The modulation characteristics and periodic pulse information in the composed new signal are masked.

$$\begin{cases} s_{c1} = 3\cos(2\pi \cdot f_1 t) \times \cos(2\pi \cdot f_2 t) \\ s_{c2} = 3\cos(2\pi \cdot f_3 t) \\ s_{c3} = \sum_{i=1}^{M} 4e^{-g\times 2\pi f_n^i t} \times \sin\left(2\pi f_n^i t \times \sqrt{1-g^2}\right) \\ s_1 = s_{c1} + s_{c2} + s_{c3} \end{cases} \tag{13}$$

The simulated signal contains three components. If the modulation signal and cosine are combined into one signal, then the Fourier spectrum of the new signal has high amplitude in two frequency bands within 1000 Hz. The energy of the Fourier spectrum of the third component is concentrated around 1600 Hz. The same situation occurs in the Fourier spectrum of the signal with three components superimposed. Fig. 3 shows the Fourier spectrum and PSD of the signal.

The Fourier spectrum can accurately represent the details of the frequency components in the signal, which provides great convenience for the analysis process, but also brings difficulties to the most critical step in EWT. The simulated signal does not contain noise, but there are many extreme points in the Fourier spectrum. The number of extreme points affects the scale space representation method, which is the main factor that causes invalid components and modal aliasing. In Fig. 3, it can be found that PSD is smoother and contains fewer extreme points than Fourier spectrum; the modulation signal and cosine signal can be separated; for periodic pulse information, PSD contains most of the energy. When all the components are superimposed, they can also be separated. As the number of extreme points of the PSD decreases, the part with lower energy would be suppressed, and the part with higher energy would be retained. The PSD-based method can obtain fewer and more reasonable boundaries.

Add 5 dB Gaussian noise to the signal shown in Eq.13. Fig. 4 shows the waveform, Fourier spectrum and PSD.

Due to the increased noise in the signal, 835 extreme points appear in the Fourier spectrum. These extreme points will interfere with the calculation process of EWT, affect the judgment of the segmentation method and shift the position of the boundaries. The PSD used in this paper only obtains 19 minimum values, retains the larger amplitude components in the original signal, and suppresses noise. Therefore, this paper proposes an adaptive spectral segmentation method and names it

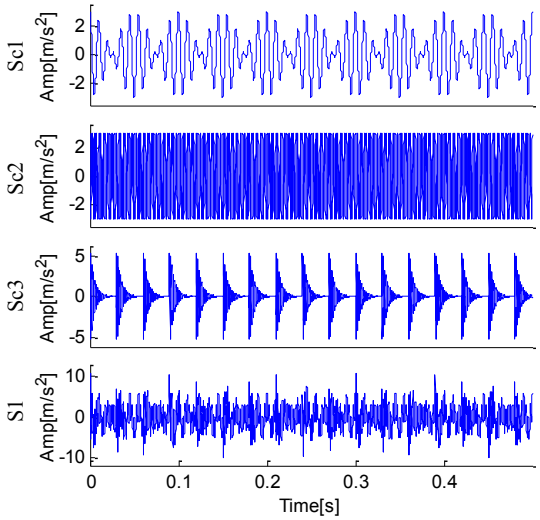

Fig. 2. Three components and synthesized simulation signal.

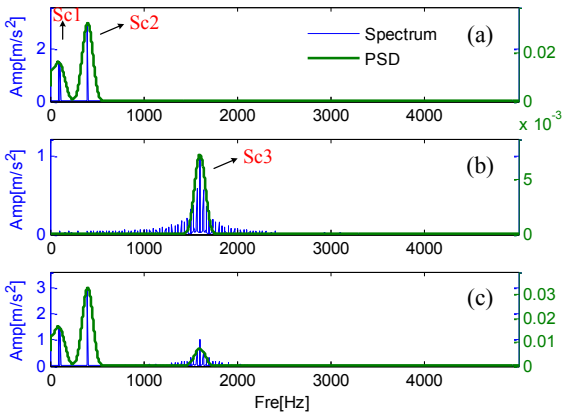

Fig. 3. Spectrum and PSD representation: (a) The spectrum of the signal composed of s_{c1} and s_{c2}; (b) The spectrum of the signal composed of s_{c3}; (c) The spectrum of the signal composed of s_1.

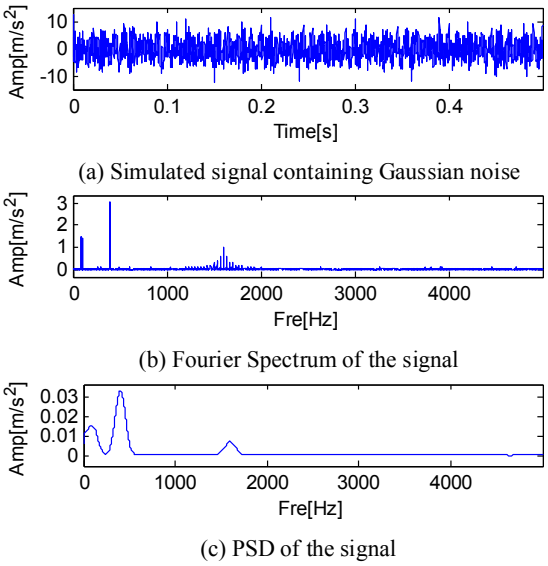

(a) Simulated signal containing Gaussian noise

(b) Fourier Spectrum of the signal

(c) PSD of the signal

Fig. 4. Simulated signal and its spectrum and PSD.

as the adaptive and concise empirical wavelet transform. The steps can be described as follows:

1. 1 Estimate the PSD of the signal based on Welch's method.
2. Normalize the PSD of the signal to the frequency range $[0, \pi]$. There are fewer extreme points in the PSD, so there is no need to use the complex scale-space representation method in the original method. This paper uses the minimum value in the PSD to obtain the boundaries. The boundaries in the range $[0, \pi]$ can divide the same position in the Fourier spectrum into several components.
3. Construct filter bank based on empirical scale function and empirical wavelet function. Each individual filter in the filter bank represents an independent component. All components make up the original signal.
4. Reconstruct the information in each filter. The original signal will be decomposed into several components located in different frequency bands.

Use the method just mentioned and the original EWT to process the signal that containing noise. It can be found from Fig. 5 that ACEWT can separate the modulated signal (A) and the cosine signal (B), and the integrity of the periodic pulse information (C) could be preserved. If the

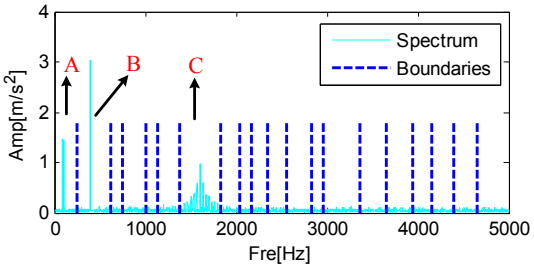

(a) Boundaries processed by ACEWT

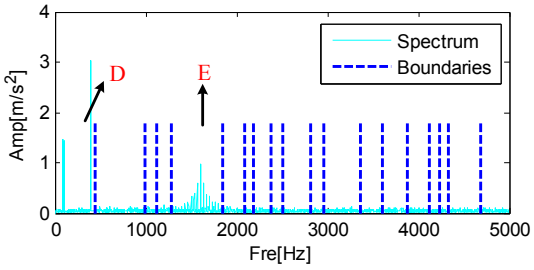

(b) Boundaries processed by EWT

Fig. 5. The comparison of two spectral segmentation methods.

original EWT method is used to process the signal, the modulation information and cosine may not be separated (D). The frequency band representing the periodic pulses (E) contains more noise.

In order to verify the accuracy of ACEWT's results, component A and B representing the modulation signal and cosine signal are used to compare with the original components. Fig. 6 shows the results of ACEWT: component A and component B are extracted. Component A and B are similar to Sc1 and Sc2 in Fig. 2. After amplifying the component A for 0.13 s-0.28 s, it can be known that they have a high degree of fit. After amplifying the component B for 0.21 s-0.25 s, it can be known that it is similar to Sc2. Therefore, the decomposition results of ACEWT are effective. Since component D obtained by EWT does not separate the modulated signal from the cosine signal, it will not be further analyzed.

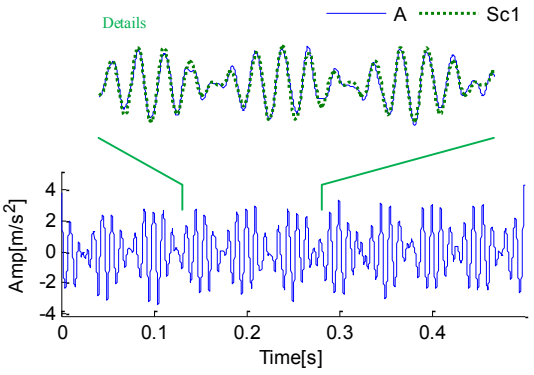

(a) Component A and its details

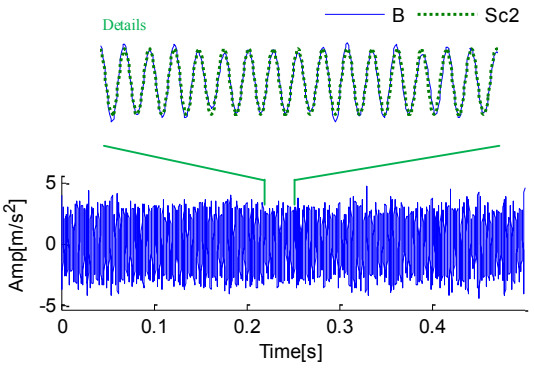

(b) Component B and its details

Fig. 6. The results decomposed by ACEWT.

For components C and E (Fig. 7), this paper verified the amount of noise contained in the signal through signal-to-noise ratio (SNR) and the similarity between the signal and the original component through root mean square (RMS). Both of these components are frequency bands where periodic pulse information is located. Although the positions of the boundaries are close, it can still be found from Table 1 that a higher SNR of component C means less noise is included; the smaller RMS of component C means that it is more similar to the original component.

Next, the characteristics of the filter should be verified. During the filtering process of EWT, the filter bank based on Meyer wavelet has good filtering characteristics. EWT can not only ensure that the information in the frequency band is not lost, but also ensure that the energy outside the frequency band is rarely leaked. Wavelet packet transform (WPT) is used to set off the filtering effect of ACEWT. Take the above signal and the extracted periodic pulse frequency band as an example. When WPT is running, the position of the boundaries is fixed. The boundaries of ACEWT could be set arbitrarily, with a higher degree of freedom. According to the habit of WPT, the left and right bound are set to: Left bound = 1250 Hz, Right bound = 1875 Hz.

Fig. 8a shows the location of the boundaries, the spectrum of the original signal and the extracted components. The results of WPT filtering are different from ACEWT in detail. Fig. 8b-e shows the relationship among the spectrum of the components extracted by the two methods and the spectrum of the original signal. It can be found that in the results obtained by the WPT, there is a lot of energy leakage in the parts below the left bound and above the right bound. In the result of the ACEWT process, the energy leakage is less in the part whose frequency is lower than the left bound or higher than the right bound.

Table 2 summarizes the energy leakage data of the above filtering results. It can be found that ACEWT leaks less energy than WPT. Within the band, the energy lost by the two methods is almost same. However, after calculating the mean square error between the signal in the frequency band and the original signal, it can be found that the error obtained by ACEWT is smaller.

3.2. *Weighted unbiased autocorrelation (WAC)*

The ACEWT proposed in this paper can divide the signal into several components, and researchers can extract parts with different characteristics according to their own needs. When a rotating machine such as

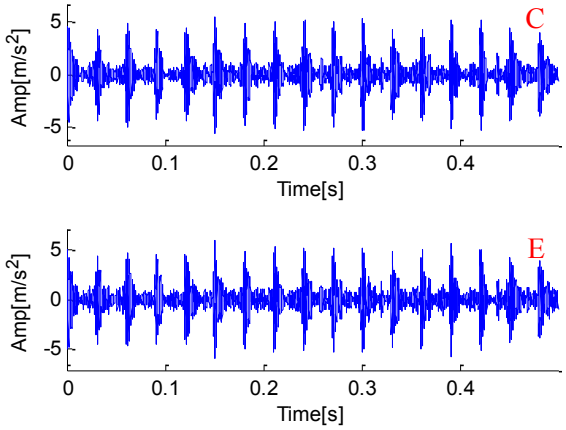

Fig. 7. Component C and E decomposed by ACEWT and EWT.

Table 1
SNR and RMS of component C and E.

Component	Method	SNR(dB)	RMS
C	ACEWT	6.24	0.6014
E	EWT	5.95	0.6220

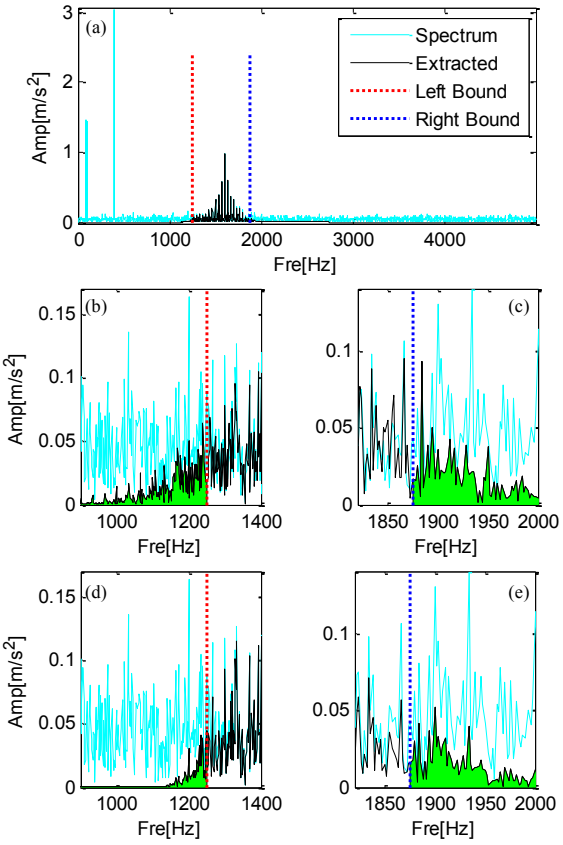

Fig. 8. The comparison of filtering effects: (a) Segmented method; (b) Left part of WPT; (c) Right part of WPT; (d) Left part of ACEWT; (e) Right part of ACEWT.

Table 2
Comparison of WPT and ACEWT filtering effects.

Method	Energy leakage %			RMS %
	Left	Right	Middle	(Middle)
ACEWT	8.62	4.34	0.48	5.83
WPT	13.33	6.14	0.47	8.66

a rolling bearing fails, the signal is usually regular. No matter the inner ring or the outer ring is damaged, the balls in the bearing will sequentially contact the location of the damage. If the speed is constant, the pulses between balls and the damage are periodic [31]. Antoni [32] refers to the characteristics of this type of signal as cyclostationary. Usually the system has a natural frequency during operation, so the fault information will concentrate near the natural frequency [24]. ACEWT proposed in this paper will obtain a set of empirical modes when processing noise and non-stationary signals. Natural frequencies and their side bands are treated as the same component. Therefore, it is necessary to automatically identify the cyclostationary information in the results.

The unbiased autocorrelation of the squared envelope of the demodulated signal proposed by Moshrefzadeh is sensitive to the periodic pulse characteristics, but the single pulse can also affect the sensitivity of AC. For the collected signals, noise cannot be completely avoided. Random pulses in noise are a test for AC. During the processing of noise and non-stationary signals, ACEWT may obtain components with a narrow frequency band and containing single pulses, which may make it difficult to screen for fault information. Even if the narrow frequency band contains the natural frequency(center frequency), it cannot contain more side bands, which would cause harmonics to not appear in the process of Hilbert envelope demodulation. The extreme points obtained by the PSD-based mode decomposition method proposed in Section 3.1 will accommodate more periodic pulse information, which means that there will be almost no narrow frequency band near the center frequency. So the width of the frequency band can be used as one of the references for determining how much fault information is contained in each frequency band. This paper proposes weighted unbiased autocorrelation (WAC) to screen fault information in empirical modes. It could combine the advantages of frequency bandwidth and unbiased autocorrelation to weaken non-stationary interference such as noise and single pulses that are not related to periodic pulse information influences.

For the signal $y(t)$, the n-th signal within the frequency band: $y_n(t)$. According to the content in Section 2, the n-th frequency band is $\Lambda_n = [\omega_{n-1}, \omega_n]$, $n = 1, 2, \cdots, N$, $\omega_0 = 0$, $\omega_N = \pi$. Therefore, the width of the frequency band after normalization can be expressed as: $\eta_n = \omega_n - \omega_{n-1}$. The weight of this band is:

$$\delta_n = \frac{\eta_n}{\pi} \tag{14}$$

The square envelope within Λ_n is $|y_n(t)|^2$, the square envelope is autocorrelated [33]:

$$\widehat{R}_{yy}(\tau) = \frac{1}{L-q}\sum_{i=1}^{L-q}|y_n(t_i)|^2 \cdot |y_n(t_i+\tau)|^2 \tag{15}$$

where $\tau = q/f_s$ represents the delay factor, $q = 0, 1, \cdots, L-1$, f_s is the sampling frequency, and L is the length of the signal.

The kurtosis of unbiased Autocorrelation in frequency band $\Lambda_n = [\omega_{n-1}, \omega_n]$ can be defined as:

$$\kappa_n = \frac{\sum_{i=1}^{L/2}\left[\widehat{R}_{yy}(i) - \min\left(\widehat{R}_{yy}(\tau)\right)\right]^4}{\left[\sum_{i=1}^{L/2}\left[\widehat{R}_{yy}(i) - \min\left(\widehat{R}_{yy}(\tau)\right)\right]^2\right]^2} \tag{16}$$

Therefore, the definition of weighted unbiased Autocorrelation (WAC) is as follows:

$$WAC_n = \delta_n \cdot \kappa_n = \frac{\eta_n}{\pi} \cdot \frac{\sum_{i=1}^{L/2}\left[\widehat{R}_{yy}(i) - \min\left(\widehat{R}_{yy}(\tau)\right)\right]^4}{\left[\sum_{i=1}^{L/2}\left[\widehat{R}_{yy}(i) - \min\left(\widehat{R}_{yy}(\tau)\right)\right]^2\right]^2} \tag{17}$$

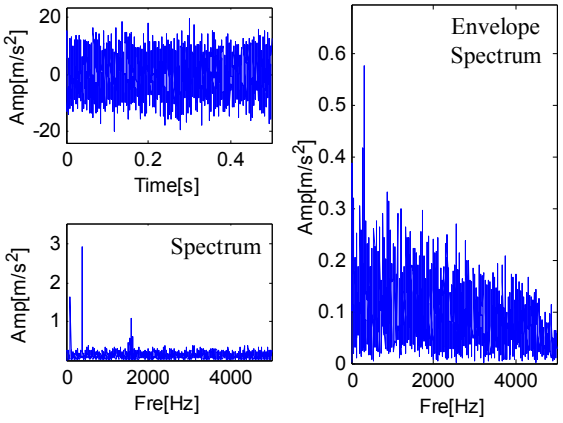

Fig. 9. Simulated signal with SNR = -5dB.

Add noise with SNR = −5dB to the signal shown in Eq.13. Fig. 9 shows the waveform, Fourier spectrum and envelope spectrum. The characteristics in the signal are difficult to discern; it is difficult to find the side band from the Fourier spectrum; the envelope spectrum is very complicated.

In order to verify the effectiveness of WAC, this section uses EWT and ACEWT to process the signal, and filter the periodic pulse information among the components by the kurtosis. Kurtosis is a statistical indicator that is sensitive to pulses, and is often used to identify whether there is a fault in the signal in bearing fault diagnosis. Fig. 10 shows the results of segmenting the spectrum by two methods. The dotted line in Fig. 10a indicates the division of the Fourier spectrum, and the dotted line in Fig. 10b indicates the division of PSD. In order to show the commonalities and differences between these two methods, PSD is not drawn in Fig. 10b but replaced by Fourier spectrum. The polyline is the kurtosis of each component; the largest kurtosis is marked by a circle. It can be found that EWT still cannot separate the modulated signal and the cosine signal. Although the fault information is concentrated at 1600 Hz, after filtering the components by the kurtosis, the center frequency of the component with the largest kurtosis is located at 3107 Hz, which deviates from the center frequency. The width of this frequency band is 110 Hz, which can only contain 3 side bands (34 Hz) at most, which will affect the envelope demodulation. ACEWT can separate the modulation signal, cosine, and frequency band containing fault information. However, the center frequency of the component obtained after filtering based on "kurtosis" is also located near 3092 Hz, and the width of this frequency band is narrow. Although the component at 1600 Hz has a wide frequency band, the pulse in the narrow frequency band affects the judgment of Kurtosis.

The two components are extracted and the waveform is shown in Fig. 11. The two components have similar center frequencies and bandwidth, so there waveforms are similar too. But the component is not periodic pulse information. The filtering method based on kurtosis selected a wrong frequency band, and the noise received by the kurtosis is relatively large. If unbiased autocorrelation is used as the screening index, EWT and ACEWT can be used to process the signal. It can be found from Fig. 12 that the AC-based filtering method has similar effects on the results of EWT, and the component at the same position is regarded as the frequency band containing more fault information.

The bandwidth of the frequency band that actually contains the most fault information is wider than that, but the AC is slightly lower. In the results obtained by ACEWT, the AC of the 23rd and 27th components is larger than the frequency band containing the most fault information, but their bandwidth is small. The maximum AC component is extracted and shown in Fig. 13. The periodic pulse contained in this component is not the most.

The weighted unbiased autocorrelation (WAC) proposed in this paper is used to identify the periodic pulse information in the components obtained by EWT and ACEWT. It can be found from Fig. 14 that both methods have successfully identified the frequency band containing the fault information. Compared with Fig. 12, WAC strengthens the AC of the wide bandwidth components and weakens the narrow bandwidth components. The two components with the largest WAC are extracted, and the waveform is shown in Fig. 15. It is easy to recognize

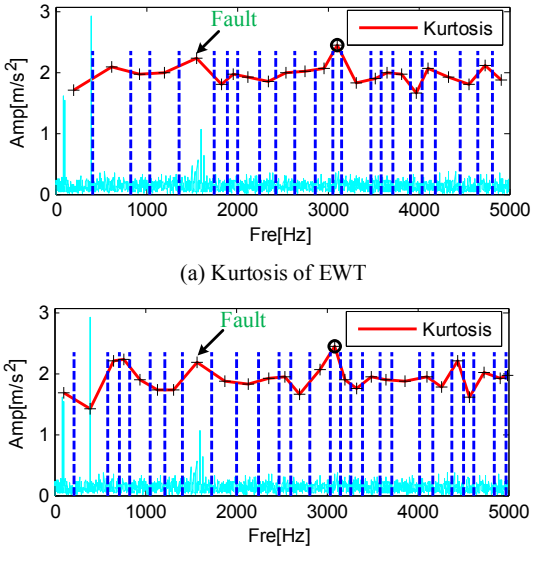

(a) Kurtosis of EWT

(b) Kurtosis of ACEWT

Fig. 10. The results recognized by kurtosis.

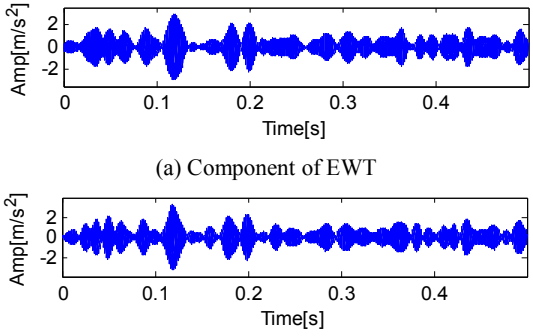

(a) Component of EWT

(b) Component of ACEWT

Fig. 11. The components with maximum kurtosis.

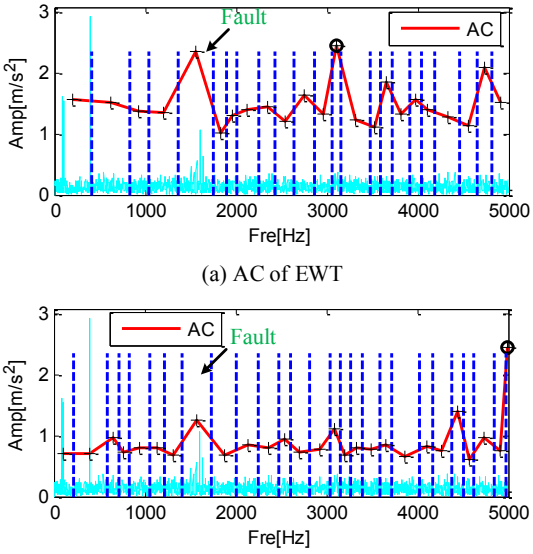

(a) AC of EWT

(b) AC of ACEWT

Fig. 12. The results recognized by AC.

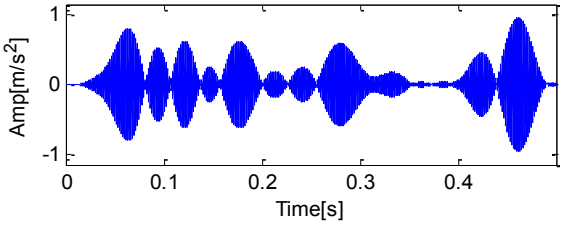

Fig. 13. The components of ACEWT with maximum AC.

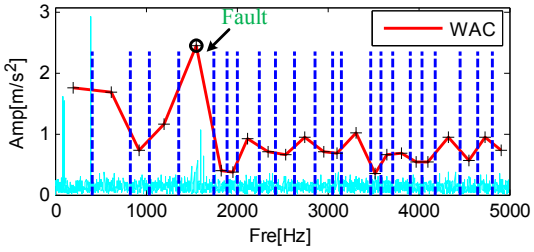

(a) WAC of EWT

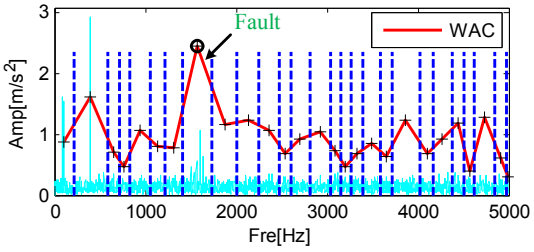

(b) WAC of ACEWT

Fig. 14. The results recognized by WAC.

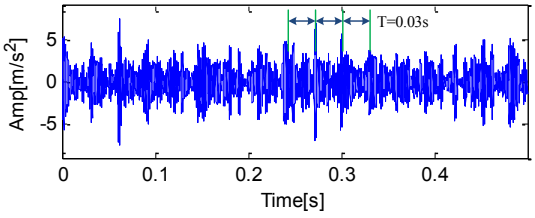

(a) Component of EWT

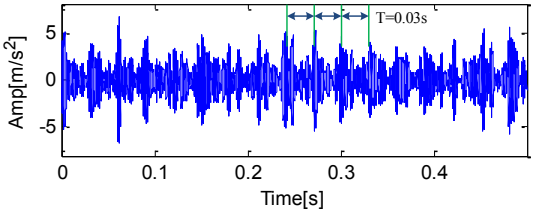

(b) Component of ACEWT

Fig. 15. The components with maximum WAC.

pulses from the waveforms of the two components, and it can be found that these pulses are periodic with T = 0.3 s, which is the same as the period of the fault information in the original signal.

This section proposed a weighted unbiased autocorrelation to screen the components of the empirical modes that may contain periodic pulses. By comparison with kurtosis and AC, it is verified that the proposed WAC can suppress the influence of single pulse on the detection index. Table 3 shows the results of the comparison of the three indicators.

3.3. W-autogram based on ACEWT and WAC

ACEWT calculates the PSD of the discrete-time signal vector via Welch's method. Hamming window would be used to estimate the final spectral. After research, the width of the Hamming window is related to the fineness of PSD.

Taking the signal shown in Eq.13 as an example, the method proposed in this paper is used to calculate PSD. If the window width is set to 5, PSD is a monotonically decreasing curve. The curve shows that the amplitude of the spectrum decreases with increasing frequency. If the window width is set to 20, the initial amplitude of the PSD is high, but two peaks and two troughs appear in the curve. The curve shows that the amplitude of the spectrum does not decrease continuously as the frequency increases. There are two parts of the energy in the spectrum that are concentrated, and the two parts of the energy are bounded by the first trough. If the window width is set to 100 or higher, the PSD becomes a more complex curve with more peaks and valleys. The curve separates the modulated signal, the cosine signal, and the frequency band containing the periodic pulse information with several troughs. The above situation is shown in Fig. 16. It can be see that the choice of the window width directly affects the fineness of the PSD, the number of boundaries and the quality of the final empirical modes.

The method proposed in this paper treats the minimum points in the PSD as boundaries to distinguish different empirical modes, and the size of the window width is related to the number and position of the boundaries. This section proposes to obtain different boundary groups by changing the window width, and combines all the boundary groups into a tower boundaries distribution diagram (W-Autogram), as shown in Fig. 17. W-Autogram is similar to the Fast Kurtogram proposed by Antoni [33–34], but with fundamental differences. The way Fast Kurtogram divides the spectrum is an average division that is not based on the actual situation of the signal. Fig. 17a is a Fast Kurtogram based on FIR, and the division method is two points and three points. Fig. 17b is a Fast Kurtogram based on STFT, and its segmentation method is approximately dichotomy. This paper proposed W-Autogram based on ACEWT and WAC. The segmentation method is related to the signal, so there is no fixed boundary position. Fig. 17c and Fig. 17d shows the relationship between the spectrum and boundaries of two different simulation signals. The number of boundaries is proportional to the window width. It can be found that the information with high amplitude and the information around it will not be separated, but will be regarded as the same component. Fast Kurtogram does not use the position of the center frequency of high-amplitude information as reference information, but divides them into several parts. In this paper, the width of the initial window is set to 5. Although the range of the window width is not

Table 3
Effectiveness of three indicators.

Method	Kurtosis	AC	WAC
EWT	X	X	○
ACEWT	X	X	○

X: Invalid ○: Effective.

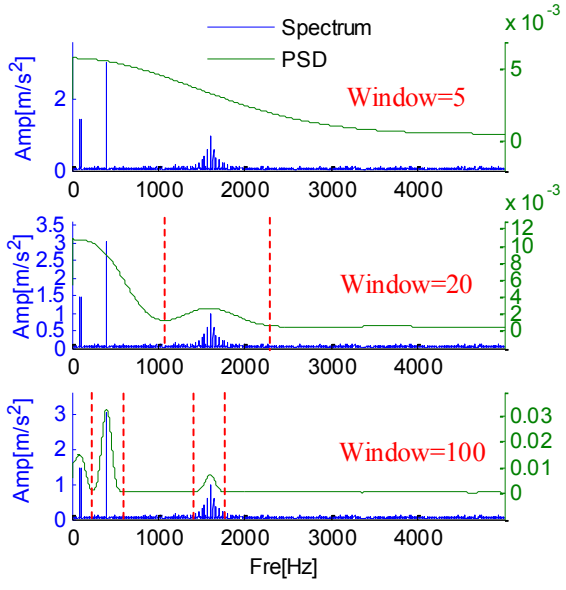

Fig. 16. The relationship between PSD and window width.

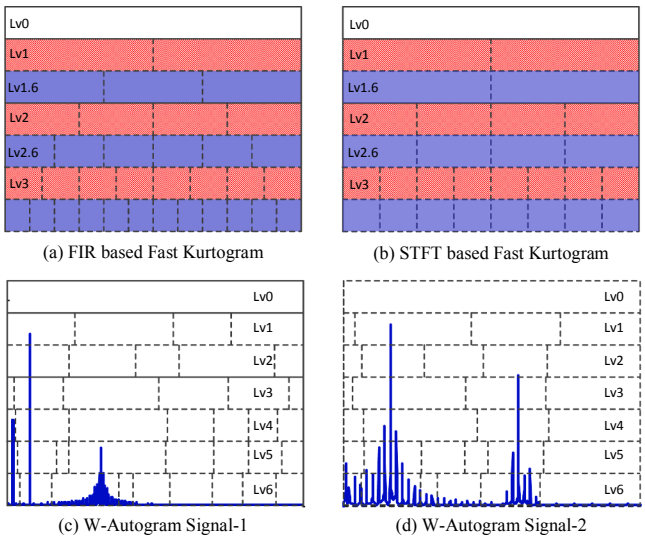

(a) FIR based Fast Kurtogram (b) STFT based Fast Kurtogram

(c) W-Autogram Signal-1 (d) W-Autogram Signal-2

Fig. 17. The demonstration of the segmentation methods of Fast Kurtogram and W-Autogram.

defined, this article defines new termination conditions: Stop when the divided frequency band is greater than 20. In the method proposed in this paper, there is no linear relationship between the number and width of frequency bands and the width of the window. Since the components in different signals are different, the PSD obtained under the same window width is generally different. Since the PSD is different, the location and number of extreme points cannot be predicted. When the window width increases, the PSD may only change slightly, the number of extreme points has not changed, but the position of the extreme points has changed. This situation arises: W-Autogram can get the same number of boundaries with different window lengths, but the bandwidth of different frequency bands is different.

A non-stationary simulation signal with strong noise is provided to verify the effectiveness of W-Autogram. The signal consists of periodic pulses s_{c1}, modulated signal s_{c2} and random noise:

$$\begin{cases} s_{c1} = \sum_{i=1}^{M} 4e^{-g\times 2\pi f_n^i t} \times \sin\left(2\pi f_n^i t \times \sqrt{1-g^2}\right) \\ s_{c2} = 2\sin(2\pi f_1 t)\sin(2\pi f_2 t + \sin(2\pi f_3 t)) \\ \quad +0.8\cos(2\pi f_4 t)\cos(2\pi f_1 t) \\ s_2 = s_{c1} + s_{c2} + \zeta \end{cases} \tag{18}$$

where, the nature frequency $f_n = 800$ Hz, the sampling frequency $f_s = 10000$ Hz, damping coefficient $g = 0.07$, and the repetition period $T = 0.01$ s. $f_1 = 50$ Hz, $f_2 = 3000$ Hz, $f_3 = 100$ Hz, $f_4 = 2$ Hz, $\zeta =$ SNR(-8dB). The waveform of the signal and its spectrum are shown in Fig. 18.

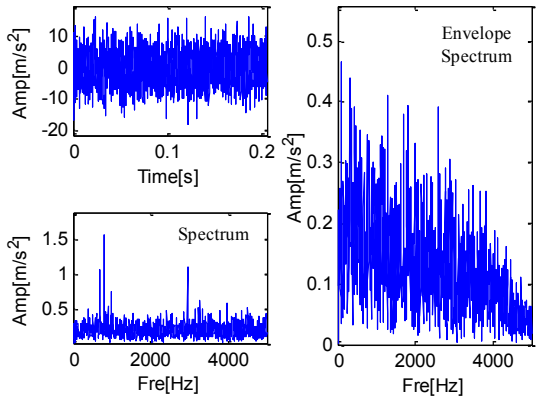

Fig. 18. Simulated signal with SNR $= -8$dB.

Due to the strong noise, it is not easy to find periodic pulses in the signal. In the Fourier spectrum, signal with a center frequency near 800 Hz might contain fault information. Fast Kurtogram was used to process the signal, and the component with the highest kurtosis is located in the first frequency band from the left in Level 3.6. The center frequency is 208 Hz and the bandwidth is 417 Hz. If Level 3.6 is expanded in Fig. 19b, the Fourier spectrum was divided into 12 parts. The kurtosis of each part is indicated by a polyline. The maximum kurtosis is marked by a circle. Eq.19b shows that the component with the center frequency at 800 is periodic pulse information and the sideband is 100 Hz. This method divides the center frequency and its sideband into two parts, so kurtosis does not detect periodic pulse information. The interference component at 3000 Hz is divided into two parts, its kurtosis is low.

In addition, the kurtosis of the first and sixth components is large, which is interfered by random components in the noise. Extracting the first component, it is not easy to find the periodic pulses from the waveform (Fig. 19c), and it is also difficult to find the characteristic frequency and harmonics from the envelope spectrum (Fig. 19d). Therefore, it is impossible to determine whether the signal contains periodic pulse information.

If the component is extracted using W-Autogram, both AC and WAC are used to filter the periodic pulse information in the components. It can be seen from Fig. 20a that although the boundary groups obtained by the two methods are the same, the fault information is judged differently by the two indicators. The largest AC in Fig. 20a1 is concentrated in the highest frequency band, while in Fig. 20a2 is concentrated around 1000 Hz. The center frequency calculated by W-Autogram is 892 Hz. According to Eq.18, it can be known that the center frequency of the fault information is 800 Hz, so the results obtained by AC may have large errors. The boundary group with a window width of 25 in Fig. 20a1 and the boundary group with a window width of 29 in Fig. 20a2 are extracted because the two components have the largest AC or WAC. The change of indicators in each frequency band is shown in Fig. 20b. After calculating the envelope spectrum of the component with the largest indicator, it can be found from Fig. 20d that the fault characteristic frequency 1/T cannot be found in the AC screening results. The WAC results include not only the fault characteristic frequency 1/T, but also harmonics. Therefore, it can be considered that the method proposed in this paper has certain advantages in extracting the periodic pulse information in the signal.

In addition, two additional experiments were used to process this signal, such as STFT-based Fast Kurtogram and Kurtosis-Autogram. Table 4 shows the processing results of the above methods. Among them, X means that the ideal result cannot be obtained, ◦ means fault information can be found, — means that it has not been verified yet.

It can be seen from Table 4 that weighting the index can improve the scope of application of the mode decomposition methods, which is effective when processing the noise and non-stationary signals such as rolling bearings of rotating machinery that may have periodic pulse information.

4. Applications

The experimental data used in this paper comes from the bearing failure test bench of Mie University, Japan, as shown in Fig. 21. The type of the bearing is NU204.

In sections 4.1 and 4.2, the inner ring fault data and outer ring fault data of the bearings are used to verify the effectiveness of the proposed methods. The location and size of the damage to the inner and outer ring are shown in Fig. 22. The inner ring of the bearing has a width of 0.5 mm and a depth of 0.15 mm. The outer ring of the bearing has a width of 0.3 mm and a depth of 0.05 mm. A static load of 150 kg was used in the experiment. The speed of shaft rotation is: 1500 rpm/s, the sampling frequency $f_s = 100$ kHz.

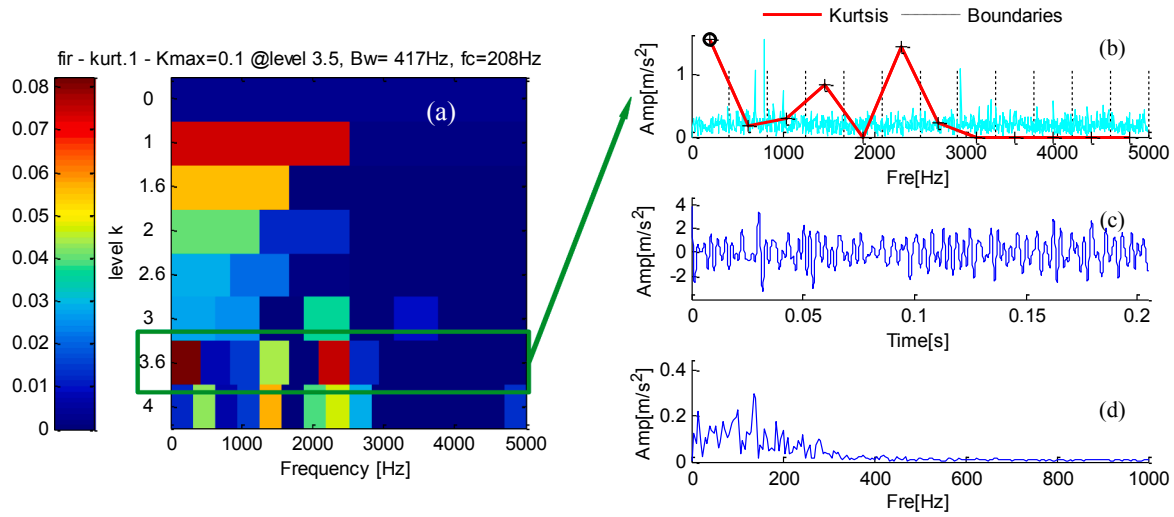

Fig. 19. Results processed by Fast Kurtogram: (a) Fast Kurtogram; (b) Boundaries and kurtosis with level 3.6; (c) The component with maximum kurtosis; (d) Envelope spectrum of the component.

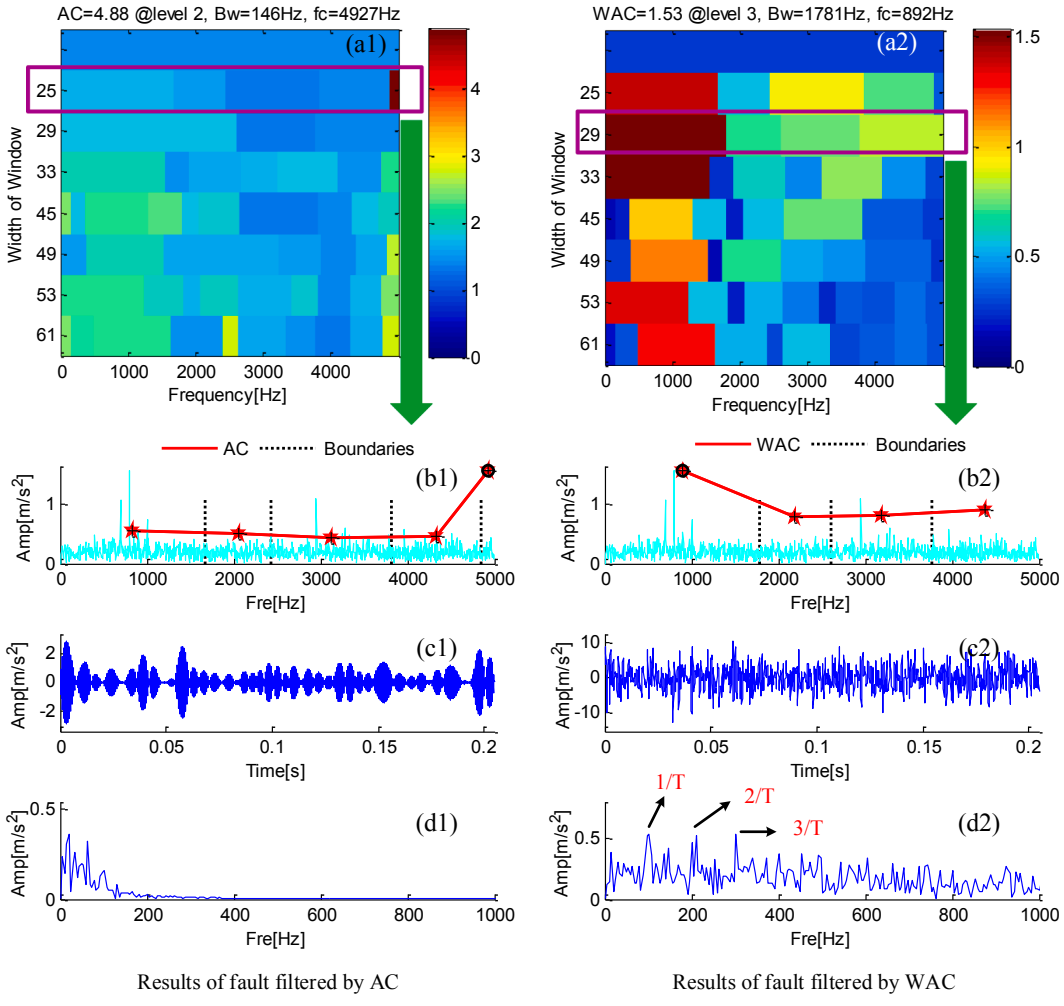

Fig. 20. The results processed by W-Autogram.
(a1) AC-Autogram; (b1) Boundaries with Window = 25; (c1) Component with maximum AC; (d1) Envelope spectrum of the component;
(a2) W-Autogram; (b2) Boundaries with Window = 29; (c2) Component with maximum WAC; (d2) Envelope spectrum of the component.

Table 4
Statistics of experimental results.

	Kurtosis	Weighted Kurtosis	AC	Weighted AC
FK-STFT	X	—	—	—
FK-FIR	X	—	—	—
W-Autogram	X	○	X	○

X: Invalid ○: Effective —: Not tested.

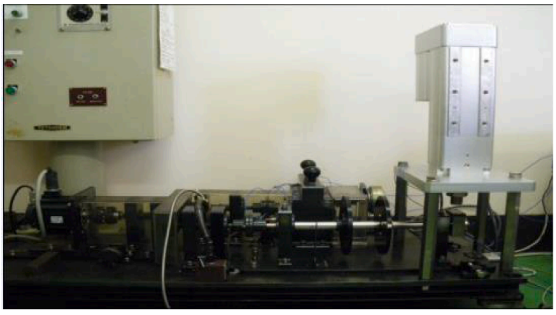

(a) Bearing test bench

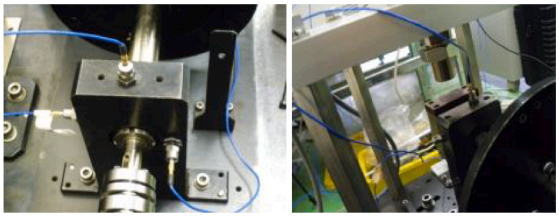

(b) Sensors

Fig. 21. Bearing test bench and the installation position of sensors.

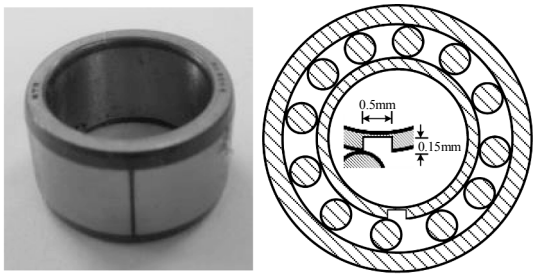

(a) Inner ring fault and the size of the damage.

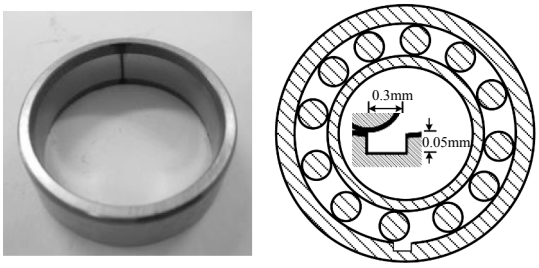

(b) Outer ring fault and the size of the damage.

Fig. 22. The location and size of the damage.

After calculation, the bearing inner ring fault characteristic frequency is $f_I = 170$ Hz, the period $T_I = 0.0059$ s. The bearing outer ring fault characteristic frequency is $f_O = 100$ Hz, the period $T_O = 0.01$ s. All information on faulty bearings can be found in Table 5.

Table 5
Details of damaged bearings.

Fault Type	Width (mm)	Depth (mm)	Statically Load (kg)	Characteristic Frequency (Hz)	Period (s)
Inner Ring	0.5	0.15	150	170	0.0059
Outer Ring	0.3	0.05	150	100	0.01

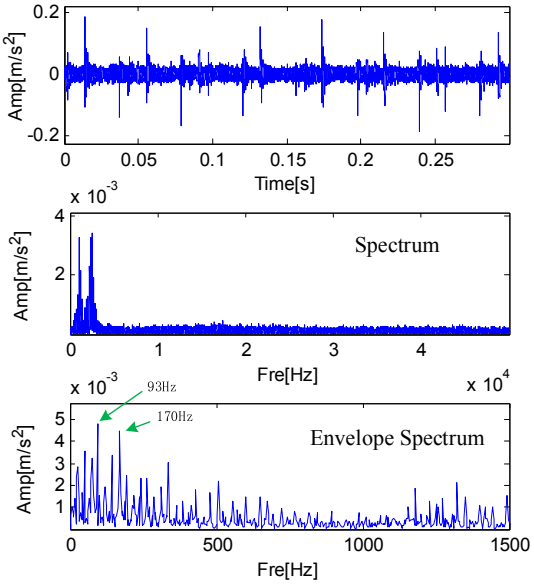

Fig. 23. The inner ring fault data, its spectrum and its envelope spectrum.

4.1. Analysis of bearing inner ring fault data

The bearing inner ring fault data, its spectrum and its envelope spectrum are shown in Fig. 23. There are noticeable pulses in the waveform. After observation, it can be found that the interval of the distribution of these pulses is longer, and the interval between different pulses is different. It is unrealistic to calculate the period of the signal. Filtering this signal can reduce the interference of noise on the fault information, which is equivalent to amplifying the periodic pulse information. For the spectrum, it can be seen that the frequency band with a frequency lower than 3 kHz has high amplitude. However, the actual situation is complicated; this part may not contain more failure information. The frequency band containing the most fault information may be masked by noise.

The results decomposed by Fast Kurtogram can be found in Fig. 24. The width of the frequency band decreases as the number of the level increases. The narrow frequency band is only related to the number of division levels, and has nothing to do with all characteristics of the signal. The highest kurtosis is located in the third band in Level 5.6. The center frequency of this band is 2604 Hz, the bandwidth is 1042 Hz, and the kurtosis is 1.8. Observe the waveform after extracting this band. There are pulses in the waveform, but there are several groups of pulses with the same period. The time interval of the marked interval in the figure can be searched in Table 6.

It can be found that only the third type of time interval is the same as the fault period of the bearing inner ring. The number of pulses with the same time interval as the third type is small and the amplitude is low. Therefore, the fault information in the extracted components is still strongly disturbed and difficult to be identified.

The original EWT will divide the spectrum into 58 parts, which consumes a lot of time. Fig. 25a shows the location and number of

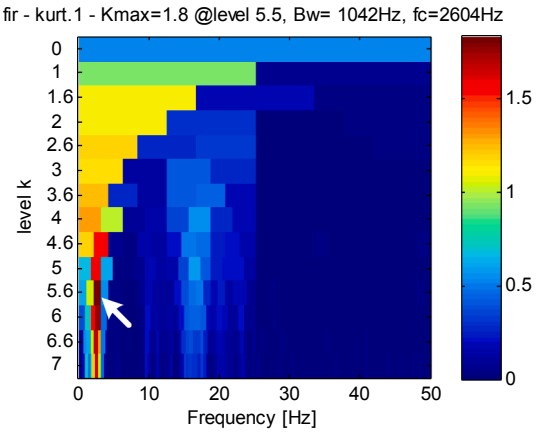

(a) Fast Kurtogram

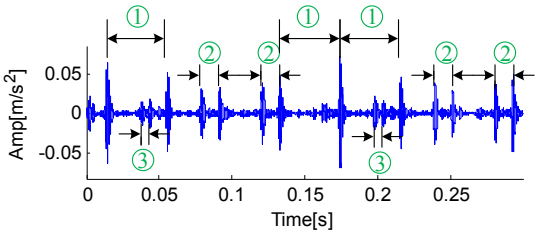

(b) Component with the maxima Kurtosis.

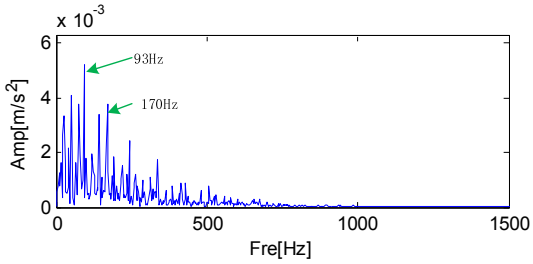

(c) Envelope spectrum of the component.

Fig. 24. The results decomposed by Fast Kurtogram.

Table 6
Time interval between pulses.

Order	1	2	3	4
	0.0415	0.0415	0.0416	—
	0.0122	0.0118	0.0121	0.0118
	0.0056	0.0060	—	—

Unit: s.

boundaries. Among them, the second component has the largest kurtosis and its waveform and envelope spectrum are shown in Fig. 25b. There is 170 Hz in the envelope spectrum, but 93 Hz and its multiples have the largest amplitude.

The W-Autogram method proposed in this paper is used to process the bearing inner ring fault data. From Fig. 26, it can be found that the part with frequency less than 10 kHz is regarded as one component in the window width variation range (17–69). The WAC in this band is less than 10 and is not the maximum at any window width. It can be judged that the fault data contained in it is not as much as Fast Kurtogram. Although the amplitude of the spectrum between 10 kHz and 30 kHz is low, W-Autogram still treats this frequency band as a component.

In Fig. 26, the largest WAC appears at Level 3, with a window width of 25, a center frequency of 21.6 kHz, and a bandwidth of 24.95 kHz. Fig. 27 displays the relationship between the spectrum and PSD when the window width is 25. There is a maximum near 17000 Hz. Since WAC

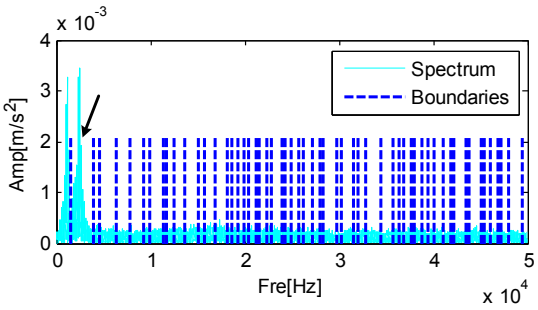

(a) Boundaries processed by EWT

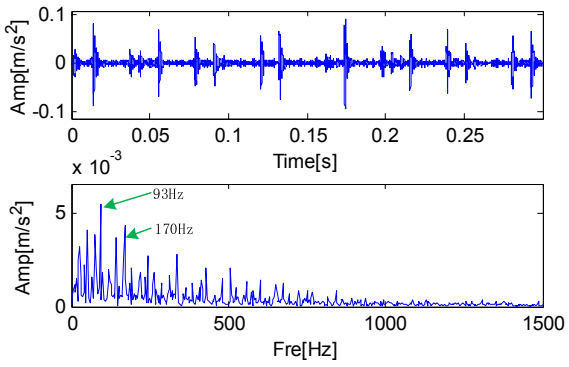

(b) Component with maxima Kurtosis

Fig. 25. The results decomposed by EWT.

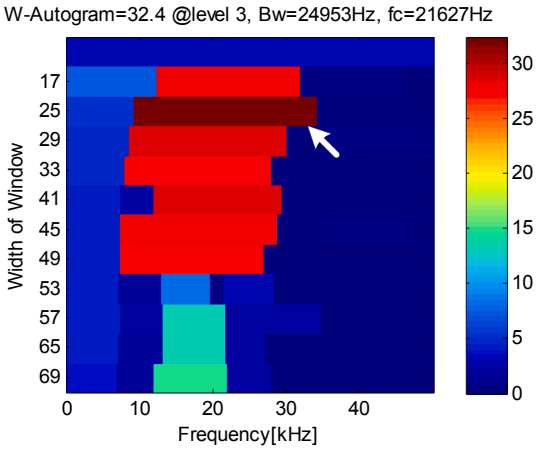

Fig. 26. The results decomposed by W-Autogram.

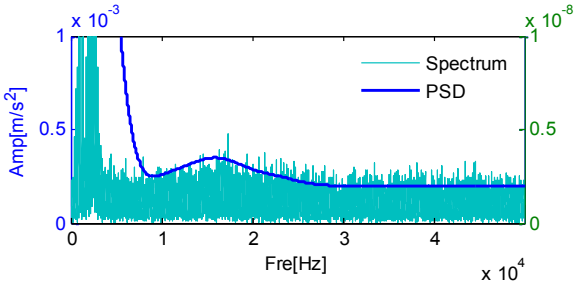

Fig. 27. The spectrum and PSD with window width = 25.

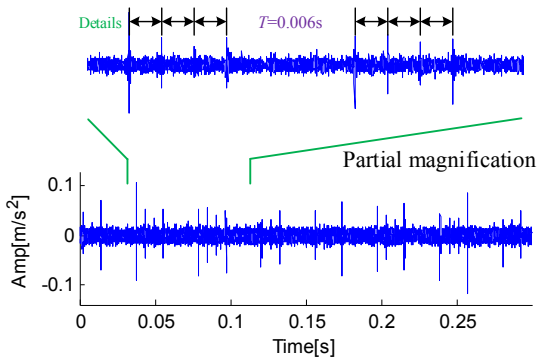

Fig. 28. The component with maximum WAC.

in this band is the largest, it is likely to contain a sideband near the maximum value representing the bearing inner ring fault information.

Extract the largest WAC component and display it in Fig. 28. The number of pulses in the signal is large and it is easy to discern periodicity. In order to show the periodicity of the pulses, the signal between 0.3 s and 0.11 s can be taken out and observed separately. Although there are no obvious pulses between 0.58 s and 0.78 s, four consecutive equally spaced pulses can be found before 0.058 s and after 0.078 s. The time interval is 0.006 s, which is equal to the failure of the bearing inner ring. Therefore, it can be judged that the signal contains the bearing inner ring fault information, and the bearing inner ring may be faulty.

In order to verify the above conclusion, Hilbert envelope demodulation can be performed on this signal (Fig. 29). It is easy to find the fault characteristic frequency of 170 Hz and its harmonics from the envelope spectrum.

Finally, the computational efficiency of EWT, Fast Kurtogram and W-Autogram is calculated. Fig. 30 shows that Fast Kurtogram is very fast. The W-Autogram proposed in this article takes 19.9425 s, which is far lower than the original EWT method.

4.2. Analysis of bearing outer ring fault data

The bearing outer ring fault data and its Fourier spectrum are shown in Fig. 31. The interference such as noise is strong, and there is no obvious pulse in the waveform. In the Fourier spectrum, the amplitudes of the signals in the entire frequency band are similar. There are no significant harmonics in the envelope spectrum. The frequency band containing the fault information is masked by strong noise.

The signal is processed by Fast Kurtogram, the results are shown in Fig. 32. The component with the highest kurtosis is located at Level 5, the seventh component from the left. The center frequency is 10156 Hz

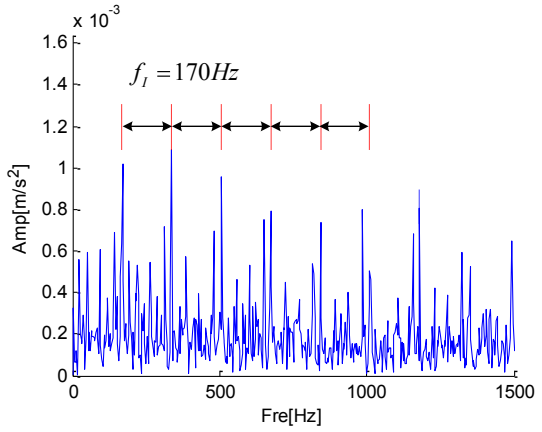

Fig. 29. Envelope spectrum of the component with maximum WAC.

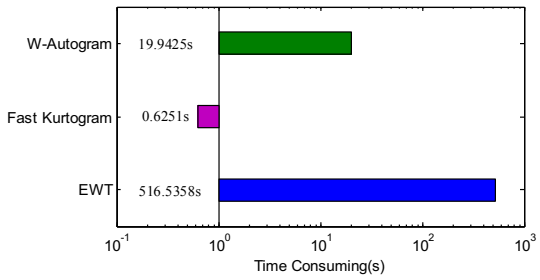

Fig. 30. Time consuming of EWT, Fast Kurtogram and W-Autogram.

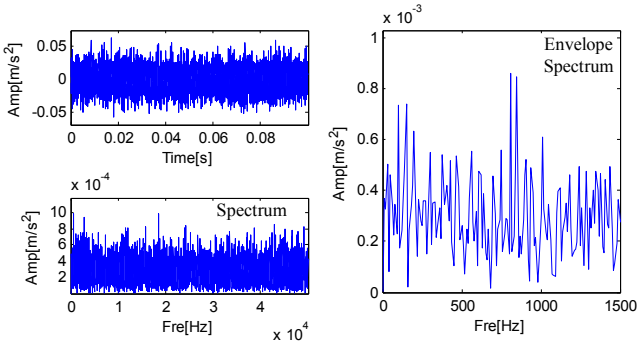

Fig. 31. The outer ring fault data, its spectrum and its envelope spectrum.

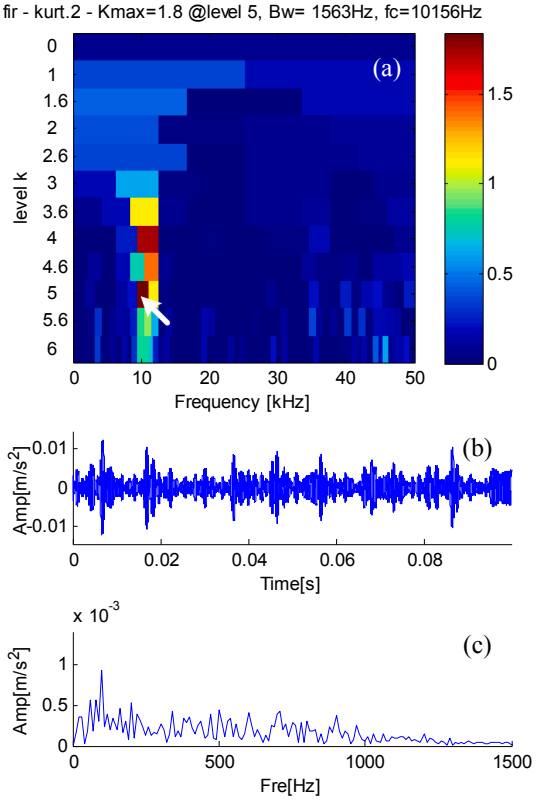

Fig. 32. The results decomposed by Fast Kurtogram: (a) Fast Kurtogram; (b) The component with maximum Kurtosis; (c) Envelope spectrum of the component.

and the bandwidth is 1563. Fig. 32b is the waveform of this component, and Fig. 32c is the envelope spectrum of the component. The width of the frequency band is small, and the extracted components exhibit the

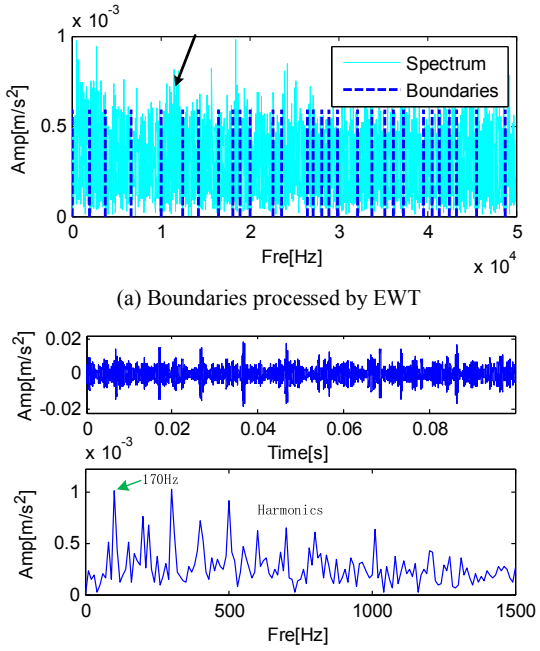

(a) Boundaries processed by EWT

(b) Component with maxima Kurtosis

Fig. 33. The results decomposed by EWT.

characteristics of an AM signal. 100 Hz can be found in the envelope spectrum, but there are no harmonics.

The original EWT will divide the spectrum into 31 parts, which consumes a lot of time. Fig. 33a shows the location and number of boundaries. Among them, the sixth component has the largest kurtosis and its waveform and envelope spectrum are shown in Fig. 33b. There is 100 Hz in the envelope spectrum.

The signal was processed by W-Autogram; the results are shown in Fig. 34. The component with the largest WAC is located at Level 10, the window width is 61, the center frequency is 10030 Hz, and the bandwidth is 6460 Hz. Fig. 34b is the waveform of this component. There are periodic pulses in the waveform of the component, and the period of the pulses is 0.01 s, which is the same as the failure period of the bearing outer ring. Fig. 34c is its envelope spectrum. There is obvious fault characteristic frequency and harmonics in the envelope spectrum. The method proposed in this paper can effectively extract the fault information in the signal of the bearing outer ring. Compared with Fast Kurtogram, the W-Autogram method proposed in this paper can collect more fault information.

Finally, the computational efficiency of EWT, Fast Kurtogram and W-Autogram is calculated. Fig. 35 shows W-Autogram proposed in this article takes 4.4086 s, which is far lower than the original EWT method.

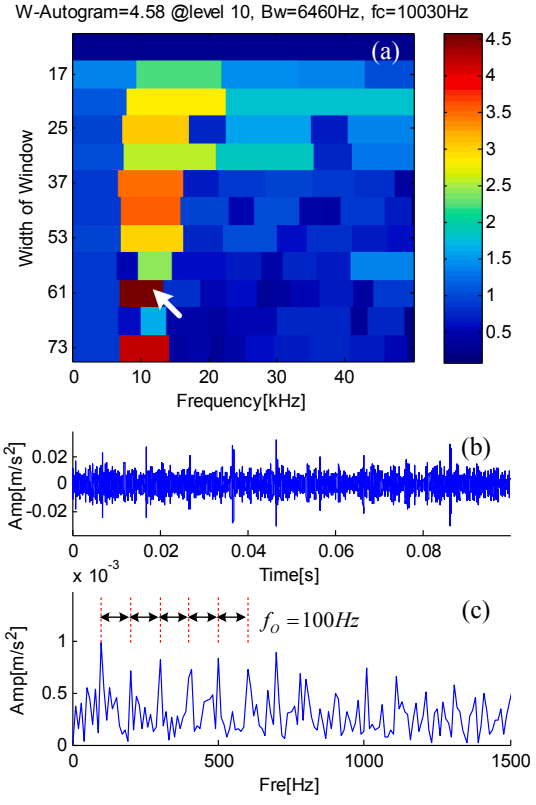

Fig. 34. The results decomposed by W-Autogram: (a) W-Autogram; (b) The component with maximum WAC; (c) Envelope spectrum of the component.

5. Conclusions

The adaptive and concise empirical wavelet transform (ACEWT) that used to reduces the original method's excessive dependence on extreme points was proposed. Simulated signals verified that the proposed method can extract different components in complex signals. Aiming at the shortcomings of indicators that are easily affected by random pulses, this paper proposed to use the bandwidth ratio to weight unbiased autocorrelation (WAC). The proposed indicator was significantly better than other indicators such as kurtosis in a strong noise environment, and the resistance to random pulses in noise was greatly increased. So it is more sensitive to periodic pulses that represent faults in rotating machinery. In order to expand the application of ACEWT, a tower boundaries distribution diagram (W-Autogram) which can be used to extract specific information is proposed by combining ACEWT and WAC. The impact of narrow bandwidth bands on indicators was reduced. The fault data of bearing inner and outer rings verified the effectiveness of the proposed method.

The method proposed in this article is not perfect, and there are some details that need further discussion or research.

1. It is necessary to further study the W-Autogram proposed in this paper. Section 3.3 states that the initial window width is 4 or 5, but the PSD obtained by the initial window width has almost no extreme points. For example, the initial window width of Fig. 20 is 25; the initial window width of Fig. 26 and Fig. 34 is 17. The reason is that the boundary group will only be displayed when the PSD has at least two minimum points. Therefore, presetting the initial window width by a suitable method can improve the efficiency of the algorithm.
2. Normally, the initial window width is set to 4 or 5. The window width gradually increases. In this case, the vertical coordinates of the W-Autogram obtained should be the same. But when the window

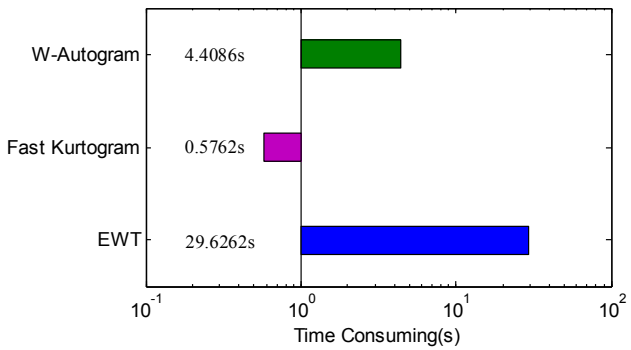

Fig. 35. Time consuming of EWT, Fast Kurtogram and W-Autogram.

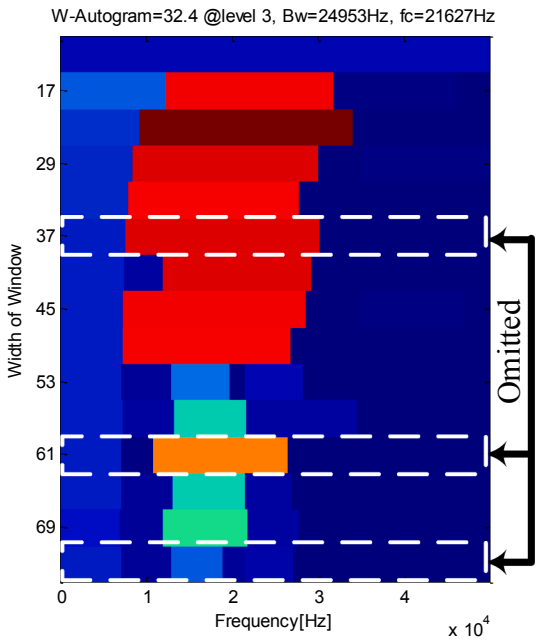

Fig. 36. The original figure before Fig. 26 is obtained.

width increases, the number and position of the boundaries may not change. Therefore, when the window width increases, if the number of boundaries is the same as before, then W-Autogram does not display the data of the window width. Fig. 36 is the original figure before Fig. 26 is obtained. Window width = 33 and 37 have the same number of boundaries; Window width = 57 and 61 have the same number of boundaries; Window width = 69 and 73 have the same number of boundaries. Therefore, the three boundary groups in Fig. 36 are deleted in this paper. When Window width = 61, a wider frequency band appears, and the WAC of this frequency band is also large. Although this value does not affect the final result, this situation deserves further study to improve the W-Autogram proposed in this paper.

Declaration of Competing Interest

The authors declared that there is no conflict of interest.

Acknowledgments

The authors would like to gratefully acknowledge Prof. Peng Chen for providing the experimental data of the bearing fault simulator and the National Natural Science Foundation of China (Grant Nos. 51775005). The authors offer sincere gratitude to the Key Laboratory of Advanced Manufacturing Technology for their support. Finally, the authors would like to thank the editors and reviewers for their valuable comments and constructive suggestions.

References

[1] L. Song, H. Wang, P. Chen, Step-by-step fuzzy diagnosis method for equipment based on symptom extraction and trivalent logic fuzzy diagnosis theory, IEEE Trans. Fuzzy Syst. (2018), https://doi.org/10.1109/TFUZZ.2018.2833820.
[2] F. Zhang, J. Huang, F. Chu, L. Cui, Mechanism and method for the full-scale quantitative diagnosis of ball bearings with an inner race fault, J. Sound Vib. 488 (2020), 115641.
[3] Z. Yan, A. Miyamoto, Z. Jiang, Frequency slice wavelet transform for transient vibration response analysis, Mech. Syst. Sig. Process. 23 (5) (2009) 1474–1489.
[4] Y. Xu, K. Zhang, C. Ma, Adaptive kurtogram and its applications in rolling bearing fault diagnosis, Mech. Syst. Sig. Process. 130 (1) (2019) 87–107.
[5] N.E. Huang, Z. Shen, S. Long, The empirical mode decomposition and the Hilbert spectrum for nonlinear and nonstationary time series analysis, Proc. Roy. Soc. London, Ser. A. 454 (1998) 903–995.
[6] H. Li, Y. Hu, F. Li, Succinct and fast empirical mode decomposition, Mech. Syst. Sig. Process. 85 (2017) 879–895.
[7] J.S. Smith, The local mean decomposition and its application to EEG perception data, J. Roy. Soc. Interface 2 (2005) 443–454.
[8] K. Zhang, Y. Xu, P. Chen, Feature extraction by enhanced analytical mode decomposition based on order statistics filter, Measurement (2020), https://doi.org/10.1016/j.measurement.2020. 108620.
[9] G. Chen, Z. Wang, A signal decomposition theorem with Hilbert transform and its application to narrowband time series with closely spaced frequency components, Mech. Syst. Sig. Process. 28 (2012) 258–279.
[10] Z. Wang, G. Chen, Analytical mode decomposition with Hilbert transform for modal parameter identification of buildings under ambient vibration, Eng. Struct. 59 (2014) 173–184.
[11] J. Gilles, Empirical wavelet transform, IEEE Trans. Signal Process. 61 (2013) 3999–4010.
[12] Y. Xu, K. Zhang, C. Ma, X. Li, J. Zhang, An Improved Empirical Wavelet Transform and Its Applications in Rolling Bearing Fault Diagnosis, Applied Sciences 8 (12) (2018) 2352.
[13] B. Premjith, M. Neethu, P. Prabaharan, K. Soman, Audio data Authentication with PMU data and EWT, Procedia Technol. 21 (2015) 596–603.
[14] Y. Jiang, H. Zhu, Z. Li, A new compound faults detection method for rolling bearings based on empirical wavelet transform and chaotic oscillator, Chaos, Solitons Fractals 89 (2016) 8–19.
[15] P. Maya, S. Vidyashree, K. Roopasree, K.P. Somanc, Discrimination of internal fault current and inrush current in a power transformer using empirical wavelet transform, Procedia Technol. 21 (2015) 514–519.
[16] W. Chen, H. Song, Automatic noise attenuation based on clustering and empirical wavelet transform, J. Appl. Geophys. 159 (2018) 649–665.
[17] T. Prabhakar, P. Geetha, Two-dimensional empirical wavelet transform based supervised hyperspectral image classification, ISPRS J. Photogramm. Remote Sens. 133 (2017) 37–45.
[18] T. Liu, J. Li, X. Cai, S. Yan, A time-frequency analysis algorithm for ultrasonic waves generating from a debonding defect by using empirical wavelet transform, Appl. Acoust. 131 (2018) 16–27.
[19] J. Chen, J. Pan, Z. Li, Generator bearing fault diagnosis for wind turbine via empirical wavelet transform using measured vibration signals, Renew. Energy 89 (2015) 80–92.
[20] W. Deng, S. Zhang, H. Zhao, X. Yang, A novel fault diagnosis method based on integrating empirical wavelet transform and fuzzy entropy for motor bearing, IEEE Access 6 (2018) 35042–35056.
[21] Y. Hu, X. Tu, F. Li, An adaptive and tacholess order analysis method based on enhanced empirical wavelet transform for fault detection of bearings with varying speeds, J. Sound Vib. 409 (2017) 241–255.
[22] D. Wang, Y. Zhao, C. Yi, Sparsity guided empirical wavelet transform for fault diagnosis of rolling element bearings, Mech. Syst. Sig. Process. 101 (2017) 292–308.
[23] M. Kedadouche, M. Thomas, A. Tahan, A comparative study between empirical wavelet transforms and empirical mode decomposition methods: Application to bearing defect diagnosis, Mech. Syst. Sig. Process. 81 (2016) 88–107.
[24] Y. Xu, K. Zhang, C. Ma, Z. Sheng, H. Shen, An Adaptive Spectrum Segmentation Method to Optimize Empirical Wavelet Transform for Rolling Bearings Fault Diagnosis, IEEE Access 7 (2019) 30437–30456.
[25] J. Gilles, K. Heal, A parameterless scale-space approach to find meaningful modes in histograms - Application to image and spectrum segmentation, Int. J. Wavelets Multire solution Inf. Process. 12 (6) (2014) 1–17.
[26] Y. Song, S. Zeng, J. Ma, A fault diagnosis method for roller bearing based on empirical wavelet transform decomposition with adaptive empirical mode segmentation, Measurement 117 (2018) 266–276.
[27] J. Zheng, H. Pan, S. Yang, Adaptive parameterless empirical wavelet transform based time-frequency analysis method and its application to rotor rubbing fault diagnosis, Signal Process., (130) (2017) 305-314.
[28] J. Pan, J. Chen, Y. Zi, Mono-component feature extraction for mechanical fault diagnosis using modified empirical wavelet transform via data-driven adaptive Fourier spectrum segment, Mech. Syst. Sig. Process. 72 (2015) 160–183.
[29] J. Amezquita-Sanchez, H. Adeli, A new music-empirical wavelet transform methodology for time–frequency analysis of noisy nonlinear and non-stationary signals, Digit. Signal Process 45 (2015) 55–68.
[30] A. Moshrefzadeh, A. Fasana, The Autogram: An effective approach for selecting the optimal demodulation band in rolling element bearings diagnosis, Mech. Syst. Sig. Process. 105 (2018) 294–318.
[31] D. Krapf, E. Marinari, R. Metzler, G. Oshanin, X. Xu, A. Squarcini, Power spectral density of a single Brownian trajectory: what one can and cannot learn from it, New J. Phys. 20 (2018), 023029.
[32] F. Zhang, J. Huang, F. Chu, L. Cui, Mechanism and Method for Outer Raceway Defect Localization of Ball Bearings, IEEE Access 8 (2020) 4351–4360.
[33] J. Antoni, The infogram: Entropic evidence of the signature of repetitive transients, Mech. Syst. Sig. Process. 74 (1) (2016) 73–94.
[34] J. Antoni, R.B. Randall, The spectral kurtosis: application to the vibratory surveillance and diagnostics of rotating machines, Mech. Syst. Sig. Process. 20 (2) (2006) 308–331.